JACS Au
AN OPEN ACCESS JOURNAL OF THE AMERICAN CHEMICAL SOCIETY

pubs.acs.org/jacsau
Article

Rational Design of Pyrido[3,2-*b*]indolizine as a Tunable Fluorescent Scaffold for Fluorogenic Bioimaging

Sihyeong Yi, Dahham Kim, Wansang Cho, Jung Ho Lee, Ji Hoon Kwon, Jonghoon Kim,* and Seung Bum Park*

Cite This: *JACS Au* 2024, 4, 2896−2906
Read Online
ACCESS | Metrics & More | Article Recommendations | Supporting Information

ABSTRACT: Novel fluorescent scaffolds are highly demanding for a wide range of applications in biomedical investigation. To meet this demand, the pyrido[3,2-*b*]indolizine scaffold was designed as a versatile organic fluorophore. With the aid of computational modeling, fluorophores offering tunable emission colors (blue to red) were constructed. Notably, constructed fluorophores absorb lights in the visible range (>400 nm) despite their small sizes (<300 g/mol). Among the fluorophores was discovered a highly fluorogenic fluorophore with a unique turn-on property, **1**, and it was developed into a washing-free bioprobe for visualizing cellular lipid droplets in living cells. Furthermore, motivated by the core's compact size and structural analogy to indole, unprecedented tryptophan-analogous fluorogenic unnatural amino acids were constructed and incorporated into fluorogenic peptide probes for monitoring peptide−protein interactions.

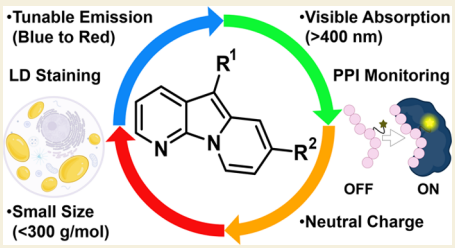

KEYWORDS: *fluorescence, rational design, photophysical properties, lipid droplet probe, fluorogenic unnatural amino acid*

1. INTRODUCTION

Since Herschel's discovery of quinine sulfate's fluorescence[1] and its subsequent explanation by Stokes,[2] organic fluorophores have garnered significant interest across various research fields. The versatility of fluorophores has been demonstrated in a wide range of applications, including bioprobes,[3,4] chemosensors,[5] chemodosimeters,[6] and organic light-emitting diodes.[7,8] Particularly in biological research, fluorescent probes have become indispensable, serving functions ranging from the selective visualization of specific organelles[9] to the real-time monitoring of biological events.[10] This broad applicability has led to a high demand for novel fluorescent core skeletons suitable for specific purposes, designed specifically for the detailed understanding of biological processes.[11−15] Environment-sensing fluorogenicity is one of the unique fluorescence properties of organic fluorophores, enabling the detection of diverse environmental changes, including hydrophobicity, viscosity, pH, and specific ion concentration, through alterations in brightness or colors.[16] These detectable changes play a crucial role in defining the overall utility of organic fluorophores. Fluorescent sensors for viscosity or hydrophobicity have been employed to monitor target engagement of drug molecules,[17] protein−protein interactions,[18] and hydrophobic organelles.[19] Despite these advancements, the utility of organic fluorophores is largely limited to existing core structures and their analogs, as designing new organic fluorophores with desired photophysical properties remains quite challenging.

To address these unmet needs, we aimed to generate a novel and biocompatible fluorophore for visualizing biological systems. In this study, we established three design criteria to ensure the effectiveness and applicability of the new organic fluorophore with high biocompatibility (Figure 1a). The primary criterion is the creation of a neutral scaffold rather than a charged one. Charged molecules, especially those with negative or point charges, can render the fluorophore impermeable to cells, whereas positively charged fluorophores may predominantly localize within mitochondria.[20] Moreover, charged molecules have the potential to disrupt or bias the native biological environment upon administration.[21] Second, we focused on developing organic fluorophores capable of absorbing visible light (>400 nm) rather than ultraviolet light (UV, <400 nm). UV light, having higher energy than visible light, can damage living systems, making UV-absorbing fluorophores less suitable for biological applications. Finally, while maintaining a sufficiently conjugated π-system for visible light absorption, we aimed to develop a smaller organic fluorophore since large fluorophores often disrupt the native functions of biomolecules.[22−25]

Although conjugated π-systems enable the absorption of UV and visible light, only a small fraction of organic molecules exhibit fluorescence, and simple π-system conjugation does not guarantee the formation of an organic fluorophore. Therefore,

Received: February 14, 2024
Revised: May 24, 2024
Accepted: May 29, 2024
Published: June 10, 2024

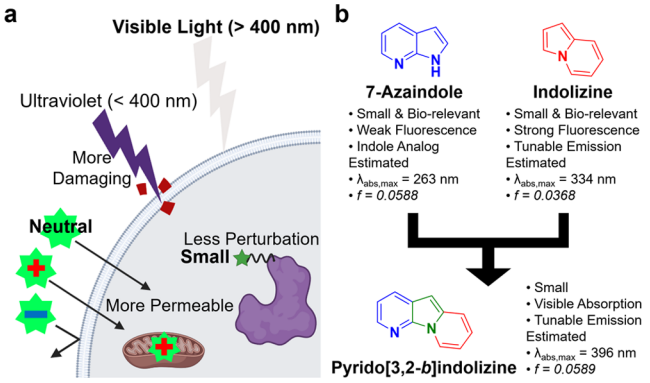

Figure 1. (a) Effects of charge, absorption wavelength, and fluorophore size on bioapplicability. (b) Characteristics of 7-azaindole and indolizine, and the rational design of pyrido[3,2-*b*]indolizine. Estimated maximum absorption wavelengths of 7-azaindole, indolizine, and pyrido[3,2-*b*]indolizine obtained by TD-DFT calculations of the corresponding first excited-state structures.

it is critical to establish a strategy that provides a novel scaffold with the designed fluorescence properties. Our approach focused on addressing the unpredictability of new organic fluorophore development by integrating two fluorophore scaffolds into one comprehensive, fully conjugated π-system rather than merely extending the π-conjugation. As a result, pyrido[3,2-*b*]indolizine was designed as a novel fluorophore scaffold by superimposing the common pyrrole motif of 7-azaindole and indolizine (Figure 1b). Of note, isomeric pyrido[2,3-*b*]indolizine derivatives were reported by Voskressensky et al., which provided further insights into the structural diversity of indolizine-based fluorophore.[26] 7-Azaindole, notable for its high biocompatibility, is recognized as a weakly fluorescent bioisostere of indole,[27−31] whereas indolizine has been used in a well-defined fluorophore, Seoul-Fluor, and extensively studied in the structure−photophysical property relationship.[32−36] Time-dependent density-functional theory (TD-DFT) calculations suggested that pyrido[3,2-*b*]indolizine would absorb light nearly in the visible range (396 nm), longer than its original components, 7-azaindole (263 nm) or indolizine (334 nm), despite its compact size.

The established design strategy allowed pyrido[3,2-*b*]-indolizine to serve as a new core scaffold, facilitating the creation of small, rigid, and neutral organic fluorophores with predictable photophysical properties and high biocompatibility, successfully meeting our three criteria. All synthesized fluorophores in this study absorb visible light (>400 nm) even though their sizes are small (mostly less than 300 g/mol). With the aid of computational calculations, optimal substituent positions were selected, enabling the fine-tuning of fluorescence colors, covering a wide visible range from blue to red.

Among these fluorophores, we discovered a highly fluorogenic (>100 folds) probe (**1**) sensing hydrophobicity via a noncanonical turn-on mechanism. Computational modeling identified the origin of its turn-on property arising from efficient dark-state quenching through the rotation and pyramidalization of the nitro group. This effective fluorogenicity led to its application in the bioimaging of lipid droplets (LDs) without washing steps.

Furthermore, encouraged by the compact size and structural similarity of pyrido[3,2-*b*]indolizine to the indole ring with its fluorogenic property, we synthetically incorporated our pyrido[3,2-*b*]indolizine scaffold into new fluorogenic unnatural amino acids, mimicking tryptophan. We also demonstrated their substantial potential in developing fluorogenic peptide-based probes to monitor peptide−protein interactions, while preserving the integrity of their innate functions and structures. The predictable photophysical property, neutral charge, small size, and structural resemblance to indole make pyrido[3,2-*b*]indolizine a biocompatible and versatile organic fluorophore with huge potential in the field of bioimaging and chemical biology.

2. RESULTS AND DISCUSSION

2.1. Rational Design of Pyrido[3,2-*b*]indolizine

We initiated the rational design of pyrido[3,2-*b*]indolizine by conducting quantum mechanical calculations to control its emission wavelength (Figure 2a). These calculations revealed

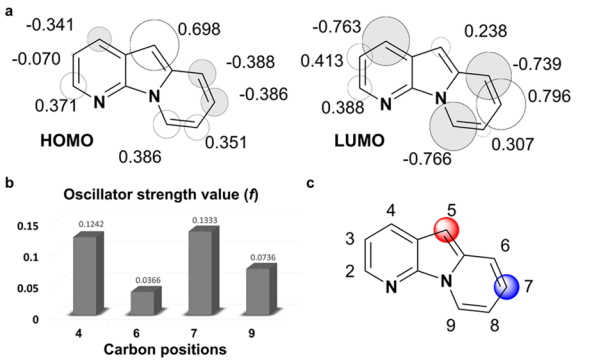

Figure 2. Structural and computational studies of the pyrido[3,2-*b*]indolizine core skeleton. (a) HOMO and LUMO coefficients for the core skeleton. (b) Calculated oscillator strengths (f) of the S0−S1 transition with the ethoxycarbonyl group incorporated at various positions. (c) Chemical structure of the pyrido[3,2-*b*]indolizine scaffold. The red circle indicates the position with the highest HOMO coefficient, while the blue circle indicates the highest LUMO coefficient.

that the C5 position is optimal for selectively perturbing the energy level of the highest occupied molecular orbital (HOMO) with a minimal impact on the energy level of the lowest unoccupied molecular orbital (LUMO), as evidenced by the large HOMO coefficient and small LUMO coefficient calculated by TD-DFT. Similarly, we selected the C4, C6, C7, and C9 positions with significant LUMO coefficients, rather than HOMO coefficients, as potential positions for various R^2 substituents. To confirm the most effective position, we calculated oscillator strengths (f), correlating with molar absorptivity (ε),[35] for the most probable S_0-S_1 transitions with pyridoindolizine analogs containing the ethoxycarbonyl moiety, one of the electron-withdrawing groups (EWGs) also serving as a versatile functional handle, at each position (Figure 2b). Among them, the C7 position was predicted to exhibit the largest f value; hence, it was chosen as the preferential LUMO controlling site. These considerations led to our final fluorophore design, a pyrido[3,2-*b*]indolizine core skeleton with R^1 and R^2 substituents at the C5 and C7 positions, respectively (Figure 2c).

The newly designed 5,7-disubstituted pyrido[3,2-*b*]-indolizine scaffold underwent retrosynthetic analysis. As illustrated in Scheme 1, the envisioned retrosynthetic pathway involved aldol condensation/cyclization, followed by oxidative aromatization. The precursors for aldol condensation were

https://doi.org/10.1021/jacsau.4c00135
JACS Au 2024, 4, 2896−2906

Scheme 1. Retrosynthetic Analysis of the Pyrido[3,2-*b*]indolizine Skeleton

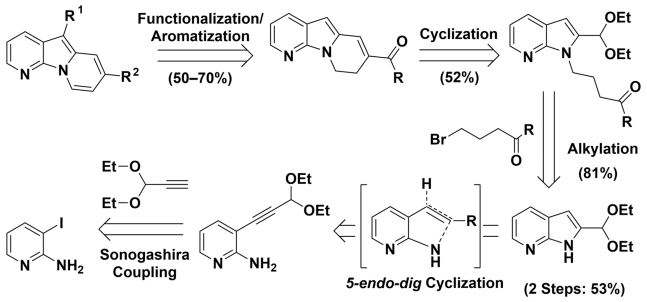

derived from *N*-alkylation and subsequent acetal deprotection of 2-diethoxy-methyl-7-azaindole, which was synthesized from 3-iodo-2-aminopyridine through Sonogashira coupling with the appropriate terminal acetylene, followed by base-promoted 5-*endo-dig* cyclization. Employing this efficient five-step synthetic pathway, we prepared a series (**1**–**15**) of 5,7-disubstituted pyrido[3,2-*b*]indolizines incorporating various substituents at the R^1 and R^2 positions.

2.2. Photophysical Properties of Pyrido[3,2-*b*]indolizines

Compounds **1**–**5**, each bearing an ethoxycarbonyl group at the R^2 position, were investigated to determine the electronic effect of the R^1 substituents on their photophysical properties. We initially hypothesized that an electron-donating group (EDG) at R^1, positioned at the most HOMO-relevant C5 carbon, would increase the HOMO energy while minimally affecting the LUMO energy, resulting in a red shift of the emission wavelength. Table 1 shows a gradual red shift of emission wavelengths from 503 to 568 nm as R^1 varied from the nitro group in **1** to the ethyl group in **5**.

On the contrary, the R^2 substituents were attached to the most LUMO-relevant C7 carbon; hence, an EDG at the R^2 position exerts the opposite effect to an EDG at R^1. With nitrile fixed as the R^1 substituent (compounds **2**, **6**–**8**), a gradual blue shift of emission wavelengths was observed ranging from 527 nm for the ethoxycarbonyl group (**2**) to 455 nm for the amino group (**6**) at R^2. Among these compounds, **8** showed exceptional water solubility, probably due to its carboxylic acid moiety. Likewise, hydrolysis of the ethoxycarbonyl moiety in **3** yielded a highly water-soluble fluorophore **9**, demonstrating notable brightness even in water (ε = 11 750 M^{-1} cm^{-1}, Φ_F = 0.49 in H_2O, Figure S1).

Interestingly, a direct comparison of each corresponding pair (**1** vs **10** and **4** vs **13**) revealed that the acetyl group (**10** and **13**), instead of the ethoxycarbonyl group (**1** and **4**) at the R^2 position, led to slightly red-shifted emissions with improved absolute brightness. Furthermore, we observed enhanced absolute brightness with a marginal change in the emission wavelength when the acetyl group (**13**) was changed to a formyl group (**14**). The introduction of a strong EWG (nitro group, **15**) at the R^2 position was found to further shift the emission toward the red color. **15** exhibited red-light emission (631 nm) with low brightness owing to strong solvatochromism in polar solvents (Figure S2). Collectively, we observed an excellent correlation between the computational predictions and the experimental observations of photophysical properties, highlighting the predictable nature of the pyrido[3,2-*b*]-indolizine scaffold (Figure S3). The normalized emission spectra of the representative pyrido[3,2-*b*]indolizine analogs **7** (blue), **1** (green), **11** (yellow), **13** (orange), and **15** (red) span the visible color range from blue to red (Figures 3a and S4). These colors are visible to the naked eyes (Figure 3b), and the synthesized fluorophores' colors are well distributed in the CIE chromaticity diagram (Figure 3c).

Table 1. Photophysical Properties of Synthesized Pyrido[3,2-*b*]indolizines[a]

cpd	R^1	R^2	λ_{abs} [nm][b]	ε [M^{-1} cm^{-1}][c]	λ_{em} [nm][d]	Φ_F[e]
1	NO_2	CO_2Et	448	16 600	503	0.41
2	CN	CO_2Et	438	8550	527	0.60
3	Ac	CO_2Et	449	8250	539	0.46
4	Br	CO_2Et	464	7800	563	0.09
5	Et	CO_2Et	470	6200	568	0.08
6	CN	NH_2	407	13 100	455	0.79
7	CN	NHBoc	410	6550	479	0.80
8	CN	CO_2H	419	6000	489	0.54
9	Ac	CO_2H	426	11 650	499	0.72
10	NO_2	Ac	453	25 000	525	0.51
11	H	Ac	445	8600	537	0.41
12	OAc	Ac	464	6200	562	0.07
13	Br	Ac	465	8200	568	0.13
14	Br	CHO	464	8750	559	0.24
15[f]	H	NO_2	487	13 450	631	0.03

[a]All experimental data were obtained in dimethylsulfoxide (DMSO). [b]The largest absorption maxima are shown. [c]Molar absorption coefficient (ε) at the maximum absorption wavelength. [d]Excited at the maximum absorption wavelength. [e]Absolute fluorescence quantum yield. [f]Photophysical properties of **15** were obtained in dichloromethane (DCM).

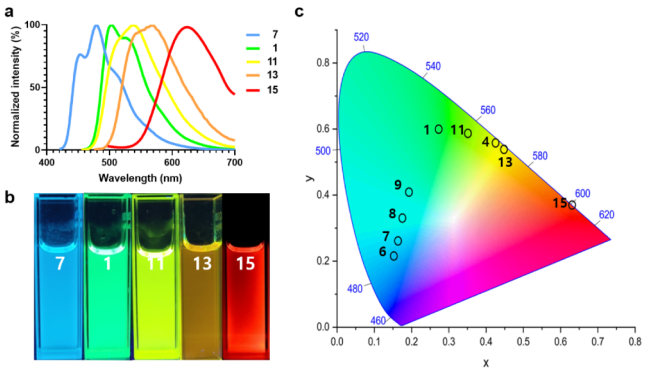

Figure 3. (a) Normalized emission spectra of representative compounds **7** (blue), **1** (green), **11** (yellow), **13** (orange), and **15** (red). (b) Fluorescence images of **7**, **1**, **11**, **13**, and **15** excited with 365 nm UV light from beneath. (c) Chromaticity coordinates of selected compounds in CIE chromaticity diagram (indicated by individually numbered spots). All spectral data were acquired in DMSO with the exception of **15** (in DCM).

2.3. Unique Turn-On Property of 1 and Its Application as a Lipid Droplet Bioprobe

Among the synthesized fluorophores, compound **1**, bearing nitro (R^1) and ethoxycarbonyl (R^2) groups, exhibited distinctive solvent-dependent turn-on behavior in a lipophilic environment, displaying over a 100-fold increase in the fluorescence intensity in diethyl ether compared to water (Figure 4a). Initially, we assumed that the general solvatochromic effect was responsible for this turn-on behavior. However, **1** showed neither a bathochromic nor a

https://doi.org/10.1021/jacsau.4c00135
JACS Au 2024, 4, 2896–2906

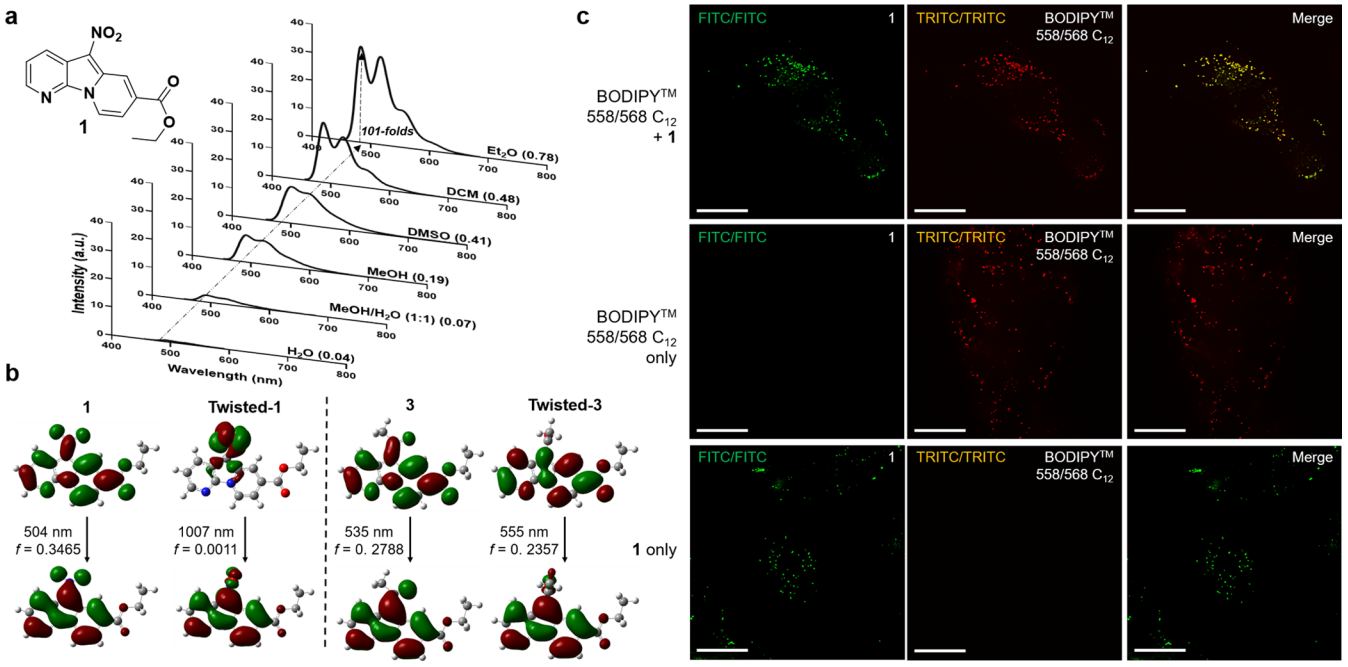

Figure 4. (a) Effect of solvent polarity on the fluorescence intensity and the quantum yield of **1**. (b) Molecular orbital distributions, calculated emission wavelengths, and oscillator strengths (f) for the S_0-S_1 transition of **1** and **3**, and their **Twisted-1** and **Twisted-3** conformers with twisted R^1 groups obtained by TD-DFT calculations (B3LYP/6-31G(d)) of the corresponding optimized first excited-state structures. (c) Colocalization of **1** with the LD-staining BODIPY 558/568 C_{12} probe in HepG2 cells. Scale bar: 15 μm.

hypsochromic shift in the emission wavelength; instead, only a change in the fluorescence intensity was observed. Interestingly, its structurally similar analog **3** did not exhibit this turn-on behavior (Figure S5), suggesting that the unique property of **1** is not caused by traditional solvatochromism.

To further investigate this phenomenon, quantum mechanical calculations were performed considering the vibrational modes of **1** and **3** (Figure S6). Surprisingly, calculations precisely reproduced the 3-peaked spectra of **1**, indicating that the observed multiple-peaked emission resulted from the vibrational modes of **1**. However, changes in solvent condition did not affect the calculated photophysical properties, implying that vibrational mode could not fully account for the solvent-dependent turn-on behavior of **1** (Figure S7). Thus, the fluorescence quenching of **1** in polar solvents is unlikely to be caused by intramolecular photoinduced electron transfer (PET), a common origin of fluorescence quenching,[30] given that pyrido[3,2-*b*]indolizine lacks a distinct PET donor or an acceptor.

We explored various theories to elucidate the unique turn-on behavior observed in **1**. In 2016, Escudero et al. reported the "dark-state quenching" mechanism as one of the origins of fluorescence quenching.[37] In this mechanism, bright S_1 ($\pi \rightarrow \pi^*$) and dark S_2 ($n \rightarrow \pi^*$) conically intersect according to the geometric changes in the fluorophore, inducing fast nonradiative relaxation of the excited state, resulting in fluorescence quenching. Larsen et al. reported a related example that the rotation and pyramidalization of the nitro group in 2-diethylamino-7-nitrofluorene (de-ANF) resulted in internal conversion (IC) between the ground and excited states.[38] The general energy level of an excited S_1 state can be stabilized in a polar solvent, facilitating IC between S_0 and S_1, leading to fluorescence quenching.

Based on these reports, we hypothesized that the unique solvent-dependent turn-on behavior of **1** arises from the rotation and pyramidalization of the nitro group. To verify this effect, a computational analysis of **1** bearing a nitro group with a 90°-twisted dihedral angle (**Twisted-1**) was performed (Figure S8). The S_0-S_1 transition in the most stable conformer of **1** showed a 504 nm emission with an oscillator strength (f) of 0.3465. In contrast, **Twisted-1** exhibited a 1007 nm emission with an f value of 0.0011 for its S_0-S_1 transition, indicating that the major S_0-S_1 transition is nonradiative. Moreover, pyramidalization of the nitro group was observed in the optimized excited-state structure of **Twisted-1**. The molecular orbital (MO) diagram also supports this hypothesis; both the MO distributions of S_0 and S_1 states of **1** were dispersed throughout the structure, whereas the S_1 state of **Twisted-1** was localized around the nitro group (Figure 4b). These findings suggest that the pyramidalization of the nitro group in **Twisted-1** stabilizes the localized MO and creates a new S_1, resulting in dark-state quenching. The newly stabilized orbital making the transition nonradiative resembles the general dark-state transition observed in several tetrazine-substituted dyes.[39,40]

In contrast, compound **3** did not display this effect (Figures 4b and S9); energy-minimized structures of both **3** and **Twisted-3** showed reasonable oscillator strength values (f) for the S_0-S_1 transitions, indicating that acetyl group rotation did not significantly affect the probability of this transition, and the S_0-S_1 transition of **Twisted-3** is radiative. These findings suggest that the unique solvent-dependent turn-on behavior of **1** originates from the rotation and pyramidalization of its nitro group, facilitated by polar solvents. This outstanding environmental sensitivity paves the way for developing **1** as a selective probe to visualize hydrophobic cellular organelles.

To validate this hypothesis, we selected a lipid droplet (LD) as a potential target organelle for probe **1** due to the hydrophobic nature of LDs.[41] Real-time monitoring of LDs in live cells is an emerging interest in the biological and

https://doi.org/10.1021/jacsau.4c00135
JACS Au 2024, 4, 2896−2906

pharmacological research communities.[42] Dynamic changes in the size and quantity of LD are closely related to metabolic syndromes, such as diabetes[43] and cardiovascular diseases,[44] as well as neurodegenerative diseases, including Alzheimer's and Huntington's diseases.[45] Prior to the practical application, we validated the photostability and cytotoxicity of **1**, ensuring its suitability for bioimaging (Figure S10). We then assessed the effectiveness of **1** as a selective LD probe in HepG2 human hepatocellular carcinoma cells. Both **1** and the well-known LD-staining probe BODIPY 558/568 C_{12} successfully visualized cellular LDs without any mutual interference in the fluorescence signals (Figure 4c).

Importantly, probe **1** enabled selective fluorescence imaging of cellular lipid droplets (LDs) without requiring washing steps, an advantage that is valuable in cell or tissue imaging, and especially in high-throughput screening. This approach enhances imaging efficiency and reduces perturbation on cells prior to imaging. Additionally, eliminating washing steps proves beneficial for in vivo tissue imaging, where such procedures may be impractical, finally leading to clearer imaging results. Further testing in HeLa human cervical cancer cells with **1** in the absence or presence of Nile Red, another widely studied LD probe, demonstrated that the fluorescence signal of **1** aligns well with that of Nile Red (Figure S11). Additionally, the signal from **1** did not colocalize with that of LysoTracker, MitoTracker, and ERTracker in HeLa cells, confirming the LD selectivity of **1** (Figure S12). On the other hand, **3** shows a dispersed fluorescence signal throughout the cell (Figure S13). These data indicate that **1** is a selective LD turn-on probe in live cells without the need for washing steps.

2.4. PPI-Monitoring Probe Using Fluorogenic Unnatural Amino Acids

Proteins play fundamental roles in both biological functions and the structural compositions of all living organisms. Typically, they do not function independently but are involved in a series of interactions with other biomacromolecules, including protein−protein or protein−peptide interactions (PPIs),[46,47] protein−RNA interactions (PRIs),[48] and protein−DNA interactions (PDIs).[49] These interactions contribute to a complex biological network called the protein interactome, which is essential in numerous biological processes. Understanding changes in these interactions during disease states can establish a solid foundation for identifying relevant genes and proteins, thus offering a new strategy for therapeutic development. Proteolysis-targeting chimeras (PROTACs) for targeted protein degradation[50] and associated bifunctional molecules[51] represent an innovative approach to artificially induce protein proximity and enhance biomacromolecule interactions. These strategies aim the specific degradation of disease-relevant target proteins, showing considerable promise for regulating interactions in disease therapeutics. As the opposite strategy, we recently reported targeted protein upregulation via the specific inhibition of the target protein and its E3 ligase interaction using small molecules.[52] Considering the pivotal role of interactomes and their regulation in biomedical research fields, visualizing these interactions is indispensable for gaining detailed insights.

Fluorescent unnatural amino acids (fUAAs) have emerged as effective tools for labeling target proteins. fUAAs can be introduced into biologically relevant peptide sequences or full-length proteins via solid-phase peptide synthesis or genetic encoding in living systems, respectively.[53] While monitoring target proteins in live cells or organisms by directly fusing fluorescent proteins is a well-estabilshed strategy for studying PPI, the genetic fusion of fluorescent proteins might disrupt the innate functions and dynamics of target proteins, owing to the comparatively large size of fluorescent proteins. In contrast, the site-specific incorporation of fUAA into target proteins or peptides allows minimal disruptions to their inherent functions and structures. The versatility of fUAAs makes them invaluable for various applications, including biomolecular assays,[54,55] synthetic biology,[56,57] and optical bioimaging,[58] ultimately enabling the direct visualization of target proteins within cellular systems. Beyond fluorescence labeling, fUAAs with environment-sensing fluorogenicity, namely fluorogenic unnatural amino acids (FUAAs), further enable background-free visualization of biomolecular interactions, especially for protein−ligand binding or PPIs. Despite several applications of fluorogenic cores (e.g., BODIPY and NBD) and their analogs in FUAAs,[59,60] the development of small and biocompatible fluorogenic unnatural amino acids remains in high demand but still presents significant challenges.

To address unmet needs, we synthesized new fluorogenic unnatural amino acids using the pyrido[3,2-*b*]indolizine scaffold. Since the improvement of the fluorescence characteristics of FUAAs has been pursued by mimicking the natural fluorescent amino acids such as tryptophan, phenylalanine, and tyrosine, the structural similarity between pyrido[3,2-*b*]-indolizine and the indole ring provides an attractive platform to synthesize unnatural analogs of tryptophan. Our approach combines the inherent biological relevance of tryptophan with the distinctive photophysical properties of pyrido[3,2-*b*]-indolizine to provide new FUAAs, leading to the creation of two distinct types of FUAAs in this study (Figure 5a). We first incorporated an amino acid framework at the C5 position of pyrido[3,2-*b*]indolizine (**17**) to preserve the connectivity of the tryptophan. Second, we attached the amino acid framework at the C3 position of **1** (**20**), which causes minimal impacts on the fluorescence property of pyrido[3,2-*b*]indolizine (Figure 2a). FUAAs (**17** and **20**) were synthesized from 5-bromo-7-acetyl pyridoindolizine (**13**) and 3-bromo-5-nitro-7-ethoxycarbonyl pyridoindolizine (**18**), respectively, by employing the Negishi coupling method.[61] As shown in Figure 5b, **17** demonstrated clear solvatochromism, while **20** exhibited photophysical properties similar to the original compound **1**, mainly featuring a unique solvent-dependent turn-on behavior (>300 fold, water to ether). These results highlight the fluorogenic potential of pyrido[3,2-*b*]indolizine-based FUAAs for developing peptide-based probes. It is worth mentioning that **17** displays outstanding photophysical properties with the reddest emission (563 nm), compared with existing tryptophan-analogous FUAAs[62−64] (Figure 5c).

To conceptually validate the utility of the designed FUAAs **17** and **20** for PPI probes, the PPI between the 95 kDa postsynaptic density protein (PSD-95) and its protein binder, Stargazin, was selected as a representative system (Figure 6a).[65−69] PSD-95 organizes signaling proteins into complexes via interactions between its PSD-95/Disc-large/Zona occluden (PDZ) domains and the C-terminal motifs of target proteins.[65] Stargazin, functioning as an auxiliary subunit of AMPAR, possesses a C-terminal motif, NTANRRTTPV, known for its binding affinity to three PDZ domains of PSD-95. Inspired by previous research by Sainlos et al.,[66] we designed and synthesized three peptide probes: **21**, **22**, and **23** (Figure 6b). The synthesis of **21** involved the modification of the lysine

https://doi.org/10.1021/jacsau.4c00135
JACS Au 2024, 4, 2896−2906

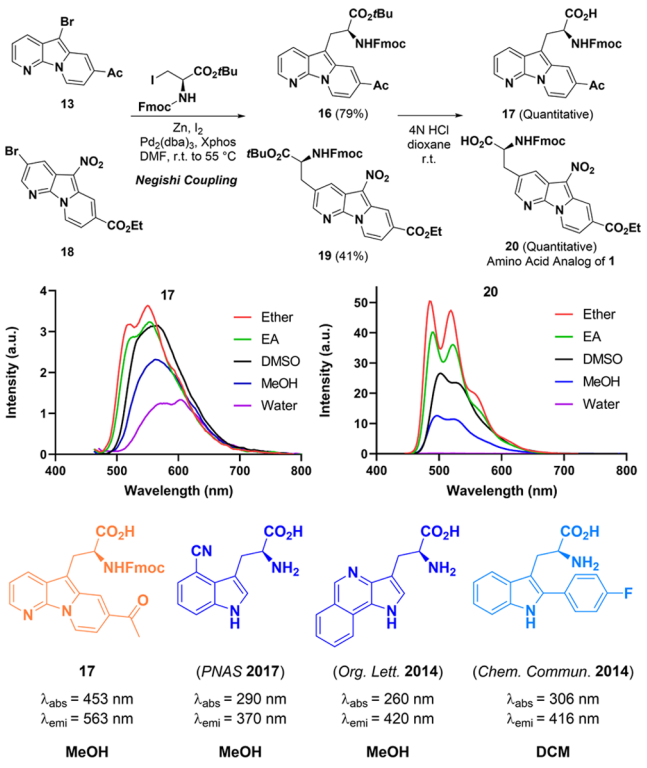

Figure 5. Fluorogenic unnatural amino acids **17** and **20**. (a) Syntheses of **17** and **20** from **13** and **18**, respectively, by the Negishi coupling and the subsequent deprotection sequence. (b) Solvent effects on the emission spectra of **17** and **20** (20 μM). (c) Comparison of photophysical properties of **17** with existing tryptophan-analogous fluorescent amino acids.[62−64]

residue in the unnatural NTANKRTTPV peptide with the NHS ester analog of **1**. Probes **22** and **23** were synthesized through Fmoc-based solid-phase peptide synthesis, introducing **17** or **20** at the first Arg position in the NTANRRTTPV sequence of Stargazin.

Among three peptide probes, **23** displayed notable turn-on properties (5.0 fold) upon interaction with the recombinant protein containing the third PDZ domain of PSD-95 (Figure 6c). **21** and **22** showed marginal turn-on ratios (2.9 and 1.4 fold, respectively) and low absolute brightness. The binding affinity of each peptide to its counterpart was measured by isothermal titration calorimetry (ITC) (Figure S14a−d). The low turn-on property of **21**, despite its strong enough binding (K_D = 2.30 μM), could be attributed to the long lysine chain detaching the fluorophore from the PPI interface. The low binding affinity of **22** correlated with its marginal turn-on property. In contrast, despite the substantial turn-on property of fluorogenic amino acid **20**, **23** showed a lower turn-on fold due to the relatively polar environment of the Stargazin−PSD-95 PPI interface.[65] In fact, the low solubility of **23** impeded the ITC experiment. These observations led us to synthesize a more soluble peptide probe **24** by incorporating three polar amino acid residues, NRR, at the *N*-terminus of **23** (Figure 6d).

The fluorescence of **24** exhibited a 5.9-fold increase in the presence of its protein counterpart (Figure 6e). The subsequent competition assay using the native Stargazin peptide (Ac-NTANRRTTPV−OH, **Ctrl**) confirmed the selectivity of **24** as a fluorogenic peptide probe for exploring interactions with PSD-95 (Figure 6f). The requirement for excess control peptide was due to the stronger binding affinity of **24** (K_D = 1.16 μM), compared to the **Ctrl** peptide (K_D = 7−15 μM, Figure S14c).[68] This proof-of-concept experiment demonstrates the potential of compact pyrido[3,2-*b*]indolizine-based FUAAs in developing fluorogenic peptide-based probes while preserving the integrity of their innate functions and structures.

3. CONCLUSION

In conclusion, we rationally designed and developed pyrido-[3,2-*b*]indolizine as a novel organic fluorophore. The synthesized fluorophores are neutral and small, with molecular weights mostly below 300 g/mol. Notably, they absorb light in the visible region (>400 nm) with tunable emission wavelengths covering a wide blue-to-red color range, thereby demonstrating the predictable photophysical properties of the pyrido[3,2-*b*]indolizine fluorophore. We also revealed the exceptional solvent-dependent turn-on behavior of compound **1**, explained its dark-state quenching by computational modeling, and developed it as a selective turn-on lipid droplet probe. Furthermore, given the compact size of pyrido[3,2-*b*]indolizine and its structural similarity to the indole ring, we synthesized fluorogenic unnatural amino acids **17** and **20**, effectively mimicking natural fluorescent amino acids such as tryptophan. Finally, we developed a peptide-based fluorogenic probe **24** with minimal interference to the functions and structures of its inherent peptide, indicating our fluorogenic amino acids' practical utility in monitoring PPIs. Overall, our research contributes to new insights into the design of novel fluorescent core skeletons and provides versatile fluorescent tools that hold promise for advancing the investigation of complex biological processes.

4. METHODS

4.1. Synthetic Procedures

All synthetic procedures are provided in the Supporting Information.

4.2. Computational Calculations

All quantum mechanical calculations were performed in Gaussian09W. The ground state structures of pyrido[3,2-*b*]indolizine, 7-azaindole, and indolizine were optimized using density functional theory (DFT) at the B3LYP/6-31G(d) level. The oscillator strength values and absorption wavelengths were calculated through time-dependent density functional theory (TD-DFT) with the optimized structures of the ground state. Atomic coefficients in the highest occupied molecular orbital (HOMO) and the lowest unoccupied molecular orbital (LUMO) of the core structure were calculated through TD-DFT at the B3LYP/6-31G*(d,p) level. The oscillator strength values of pyrido[3,2-*b*]indolizines with an ethoxycarbonyl moiety on each carbon position (C4, C6, C7, C9) were obtained through TD-DFT at the B3LYP/6-31G*(d) level. The estimated emission wavelength of each compound was calculated via optimization of the S_1 state through TD-DFT at the B3LYP/6-31G level. The estimated absorption and emission spectra of **1** and **3** considering vibrational modes were obtained with frequency calculations of **1** and **3** through TD-DFT at the B3LYP/6-31G(d) level.

4.3. Cell Culture

HepG2 human hepatocarcinoma cells were cultured in DMEM, supplemented with 10% (v/v) FBS and 1% (v/v)

https://doi.org/10.1021/jacsau.4c00135
JACS Au 2024, 4, 2896−2906

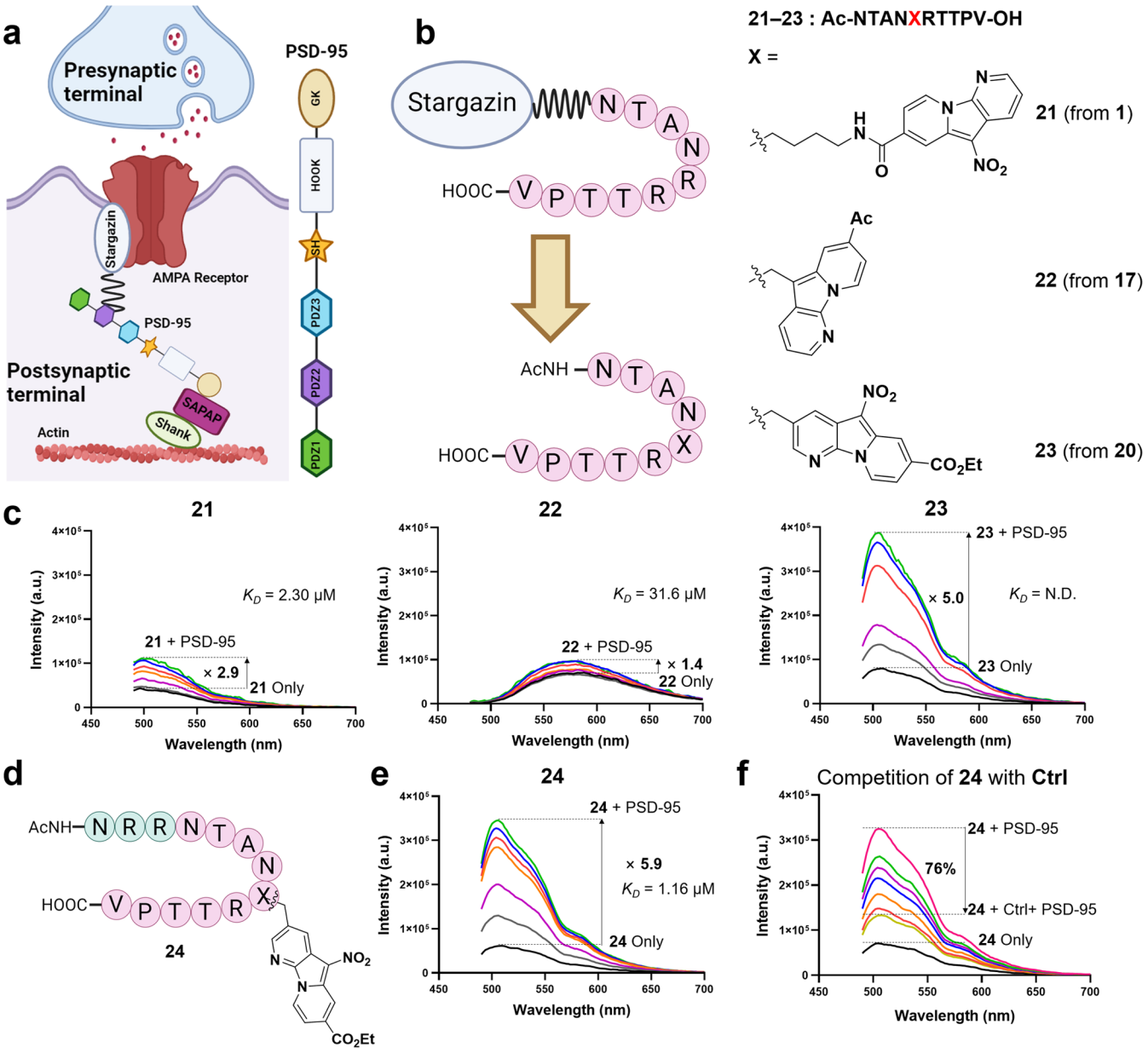

Figure 6. Development of fluorogenic peptide probes **21**–**24**. (a) Schematic biology of PSD-95 and Stargazin interaction. Reproduced with permission from [69]. Copyright [2024] [Elsevier] (b) Structures of synthesized peptides **21**–**23**. (c) Selective turn-on properties of fluorogenic probe peptides **21**–**23** (1 μM) engaged with third PDZ domain of PSD-95 (32 μM). Dissociation constants (K_D) were determined by isothermal titration calorimetry (ITC) experiments. (d) Chemical structure of the probe peptide **24**. (e) Selective turn-on property of the probe peptide **24** (1 μM) engaged with third PDZ domain of PSD-95 (32 μM). (f) Fluorescence decreases of the probe peptide **24** (1 μM) engaged with third PDZ domain of PSD-95 by competition with the soluble control peptide (**Ctrl**). Fluorescence intensities were measured with 1 μM of each peptide in PBS buffer (DMSO 5%v/v). Graph lines in (c) and (e) indicate different concentration of proteins from 0 μM to 32 μM in the power of 2 sequence. Graph lines in (f) indicate different concentration of competing peptide (NTANRRTTPV) from 0 to 200 μM with 4 μM of protein.

antibiotic-antimycotic solution. HeLa human cervical cancer cells were cultured in RPMI 1640, supplemented with 10% (v/v) FBS and 1% (v/v) antibiotic-antimycotic solution. Cells were cultured in a 100 mm culture dish and maintained in a 37 °C, 5% CO_2 incubator with a humidified atmosphere.

4.4. Fluorescence Imaging

For the costaining of lipid droplets using BODIPY 558/568 C_{12} with **1**, HepG2 cells were seeded in Nunc Lab-Tek II chambered coverglass and maintained for 1 day. Then, cells were incubated with 2 μM BODIPY 558/568 C_{12} for 16 h. After incubation, media were aspirated and refilled with 10 μM **1**-containing media or an equivalent volume of DMSO-containing media for 20 min, followed by subsequent fluorescence imaging without additional washing steps or media exchange. Fluorescence of BODIPY 558/568 C_{12} was visualized using a TRITC/TRITC filter set (λ_{ex}: 542/27 nm; λ_{em}: 597/45 nm). Fluorescence of probe **1** was visualized using a FITC/FITC filter set (λ_{ex}: 475/28 nm; λ_{em}: 525/48 nm). For the costaining experiment of lipid droplets using Nile Red in the presence of **1**, HeLa cells were seeded in Nunc Lab-Tek II chambered coverglasses and maintained for 1 day. Then, cells were incubated with 3 μM Nile Red for 20 min at 37 °C. After incubation, media was aspirated and refilled with 10 μM **1**-

https://doi.org/10.1021/jacsau.4c00135
JACS Au 2024, 4, 2896−2906

containing media or an equivalent volume of DMSO-containing media for 20 min, followed by subsequent fluorescence imaging without additional washing step or media exchange. Nile Red's fluorescence was visualized using a YFP/mCherry filter set. Fluorescence of **1** was visualized using a CFP/CFP filter set. CFP (λ_{ex}: 438/24 nm; λ_{em}: 475/24 nm), YFP (λ_{ex}: 513/17 nm), mCherry (λ_{em}: 625/45 nm). For the costaining of cellular organelles using ER-tracker Red (for endoplasmic reticulum (ER) staining), LysoTracker Deep Red (for lysosome staining), MitoTracker Deep Red FM (for mitochondria staining), respectively, in the presence of **1**, HeLa cells were seeded in Nunc Lab-Tek II chambered coverglass and maintained for 1 day. Then, cells were incubated with 1 μM ER-tracker Red for 45 min, 75 nM LysoTracker Deep Red for 45 min, 200 nM MitoTracker Deep Red FM for 20 min, respectively. After incubation at 37 °C, media was aspirated and refilled with 10 μM **1**-containing media or an equivalent volume of DMSO-containing media for 20 min, followed by subsequent fluorescence imaging without additional washing steps or media exchange. ER-tracker Red fluorescence was visualized using a TRITC/TRITC filter set (λ_{ex}: 542/27 nm; λ_{em}: 597/45 nm). The fluorescence of LysoTracker Deep Red and MitoTracker Deep Red FM were visualized using a Cy5/Cy5 filter set (λ_{ex}: 632/22 nm, λ_{em}: 679/34 nm). The fluorescence of **1** was visualized using a FITC/FITC filter set (λ_{ex}: 475/28 nm; λ_{em}: 525/48 nm). For the comparison experiment between **1** and **3** (Figrue S13), HepG2 cells were seeded in a 4-well confocal dish (SPL, Korea 214350) and maintained for 1 day. Then, cells were incubated with 3 μM Nile Red or an equivalent volume of DMSO-containing media for 20 min at 37 °C. After incubation, media were aspirated and refilled with 10 μM **1**- or **3**-containing media or an equivalent volume of DMSO-containing media for 20 min, followed by subsequent fluorescence imaging without additional washing steps or media exchange. Only for this experiment, imaging was performed with a Zeiss 980 confocal laser scanning microscope.

4.5. Photobleaching Experiment

1 (2 μM) and BODIPY 558/568 C_{12} (2 μM) in diethyl ether were exposed to 365 nm UV light under a Black-Ray B-100AP High Intensity UV Lamp (P/N 95−0127−01 M, 100 W, 365 nm, Upland, CA, USA) with a light intensity of 757 mW/cm^2. Fluorescence emission spectra were measured using a Cary Eclipse (Varian, USA) after 0, 30, 60, 120, 180, 240, and 300 min of light exposure.

4.6. Peptide Synthesis

We prepared all peptides (**Ctrl**, **21**, **22**, **23**, and **24**) via Fmoc-based solid-phase peptide synthesis using Fmoc-Val-Wang resin (100 mg, 0.38 mmol/g). First, Fmoc-Val-Wang resin was deprotected using 2 mL of 20% (v/v) piperidine in *N*,*N*-dimethylformamide (DMF). *N*-α-Fmoc−protected amino acids (0.228 mmol, 6 equiv) were conjugated to the resin using benzotriazol-1-yloxytripyrrolidinophosphonium hexafluorophosphate (PyPOB; 0.228 mmol, 6 equiv) and *N*,*N*-diisopropylethylamine (DIPEA; 0.228 mmol, 6 equiv) in 2 mL of DMF and deprotected using 2 mL of 20% piperidine in DMF. Subsequently, the coupling of amino acids and Fmoc deprotection steps were repeated sequentially until the last amino acid using a microwave peptide synthesizer (CEM, Matthews, NC, USA) with the irradiation set at 5 W for 5 min. For the acetylation of the peptide, a solution of acetic anhydride (1.9 mmol, 50 equiv) and DIPEA (1.9 mmol, 50 equiv) in 2 mL of DMF was added to the resin-bound peptide, and the same irradiation set for the coupling of the amino acids in the microwave peptide synthesizer was conducted. The peptides were cleaved from the resin with 2 mL of the solution of trifluoroacetic acid (TFA)/triisopropylsilane (TIS)/water (v/v, 95:2.5:2.5) for 2 h. After the cleavage, peptides were precipitated from diethyl ether and collected by filtration. Finally, the peptides were purified with HPLC (LC-6 AD Pump and SPD-10A detector, Shimadzu, Japan) with a YMC-Pack ODS-A C_{18} (AA12S05−2520WT, 250 × 20.0 mm I.D. S-5 μm, 12 nm) column at a flow rate of 8.0 mL/min of eluent solutions with the gradient of 10% B/A to 100% B (Solution A: water with 0.1% (v/v) TFA and Solution B: acetonitrile (ACN) with 0.1% (v/v) TFA).

4.7. Cloning – PDZ Domains and Rationale on Tandem Domain Cloning

The third PDZ domain of PSD-95 was cloned into the pETM33-Nsp1 vector (Addgene) using *NcoI* and *Eco*RI restriction sites. The third PDZ domain of PSD-95 (residues 302 to 402) was PCR-amplified using the primers 5′- CAC TAG TAG CAA TTC CAT GGA CGG TCT AGG GGA GGA AGA TAT TCC CC and 5′- AGC TTG TCG ACG GAG CTC GAA TTC CTA GGC CTC GAA TCG GCT ATA. The PCR-amplified insert was digested with either *NcoI*/*EcoRI* and ligated into a *NcoI*/*EcoRI*-digested pETM33-Nsp1 vector.

4.8. Expression and Purification of the Recombinant PDZ Domains

E. coli Rosett(DE3) cells were transformed with the third PDZ domain of PSD-95 protein expression plasmids. Cells were amplified in 0.6 L of an LB broth first at 37 °C for 5 h, followed by 16 h at 18 °C. Cells were harvested by centrifugation, and the pellet was resuspended in PBS containing protease inhibitor cocktail (Roche). Cells were lysed by ultrasonication (ULH-700S) at 40% power with a 30% duty cycle for 25 min on ice. Then, the lysate was cleared by centrifugation (11 000 g, 1 h, 4 °C). After centrifugation, the soluble supernatant was filtered and incubated with Ni-NTA beads for 1 h on ice, followed by the elution with lysis buffer containing 250 mM imidazole. Finally, buffer exchange to PBS or MES (20 mM MES, 20 mM NaCl, pH 6.0) buffer was proceeded using a PD-10 column and an Amicon Ultra 3k device. The purity of the protein was confirmed by Coomassie staining and western blot after SDS-PAGE. Protein concentrations were measured using the BCA assay (Pierce) with BSA as the reference standard or by determining the absorption at 280 nm.

4.9. Isothermal Titration Calorimetry

The PDZ domain of PSD-95 and peptides used for ITC measurements were dissolved in an assay buffer composed of pH 6.0, 10 mM MES, 20 mM NaCl, and 5% (v/v) DMSO. The PDZ domain (50 μM, 200 μL) was loaded into the sample cell, and the peptide solution (500 μM, 40 μL) was drawn into the syringe. A total of 20 injections were programmed with the first injection volume set at 0.4 μL (0.8 s duration) and the remaining at 2 μL (in 19 injections of 4 s each). The spacing between injections was 120 s. The reference power was 5 μcal/s with an initial delay of 70 s. Experiments were conducted at 25 °C with a stirring speed of 750 rpm. The raw data were collected and analyzed by Origin software (MicroCal). The binding constants were determined

https://doi.org/10.1021/jacsau.4c00135
JACS Au 2024, 4, 2896−2906

by nonlinear least-squares fitting using one set of binding sites model.

4.10. Fluorescence Measurement through Peptide and the Recombinant PDZ Domain Binding

Recombinant PDZ domain of PSD-95 was prepared as 160 μM in PBS buffer. Each fluorescent probe peptide (**21**, **22**, **23**, and **24**) was diluted from 2 mM DMSO stock solution. The control peptide (**Ctrl**) was diluted from 4 mM DMSO stock solution. For protein titration assay, fluorescent probe peptide (1 μM) and PDZ domain (0 to 32 μM) were diluted in PBS buffer with 5% (v/v) DMSO. Each solution was transferred to Corning 96-well half area black/clear flat bottom (50 μL per well). The fluorescence spectrum of each well was measured using a SpectraMax ID5 microplate reader at room temperature (RT) (450 nm excitation: **21**, **23**, and **24**, 440 nm excitation: **22**). For control peptide competition assay, **24** (1 μM), PDZ domain (4 μM), and control peptide (0 to 200 μM) were diluted in PBS buffer with 5% (v/v) DMSO. Each solution was transferred to Corning 96-well half area black/clear flat bottom (50 μL per well). The fluorescence spectrum of each well was measured using a SpectraMax ID5 microplate reader at RT (450 nm excitation).

■ ASSOCIATED CONTENT

Supporting Information

The Supporting Information is available free of charge at https://pubs.acs.org/doi/10.1021/jacsau.4c00135.

General experimental information, experimental procedures, Table S1, Figures S1−S14, synthetic procedures, absorption and emission spectra of **1**−**15**, **17**, and **20**, and $^{1}H/^{13}C$ NMR spectra of new compounds (PDF)

■ AUTHOR INFORMATION

Corresponding Authors

Jonghoon Kim − *Department of Chemistry and Integrative Institute of Basic Science, Department of Green Chemistry and Materials Engineering, Soongsil University, Seoul 06978, Korea;* orcid.org/0000-0003-4951-5497; Email: jhkim19@ssu.ac.kr

Seung Bum Park − *CRI Center for Chemical Proteomics, Department of Chemistry and Department of Biophysics and Chemical Biology, Seoul National University, Seoul 08826, Korea;* orcid.org/0000-0003-1753-1433; Email: sbpark@snu.ac.kr

Authors

Sihyeong Yi − *CRI Center for Chemical Proteomics, Department of Chemistry, Seoul National University, Seoul 08826, Korea*

Dahham Kim − *CRI Center for Chemical Proteomics, Department of Chemistry, Seoul National University, Seoul 08826, Korea;* orcid.org/0000-0002-4915-337X

Wansang Cho − *CRI Center for Chemical Proteomics, Department of Chemistry, Seoul National University, Seoul 08826, Korea;* orcid.org/0000-0002-5262-9543

Jung Ho Lee − *Department of Biophysics and Chemical Biology, Seoul National University, Seoul 08826, Korea*

Ji Hoon Kwon − *CRI Center for Chemical Proteomics, Department of Chemistry, Seoul National University, Seoul 08826, Korea*

Complete contact information is available at: https://pubs.acs.org/10.1021/jacsau.4c00135

Author Contributions

S.Y., J.K., and S.B.P. conceived and designed the project. S.Y. and J.K. performed and analyzed the experimental data. S.Y. and D.K. performed compuational time-dependent density function theory calculations. W.C. performed cellular imagings and cell viability test. J.H.L. performed *Escherichia coli* transformation and protein extraction. D.K. performed fluorescence-based plate reader experiments. J.H.K. performed isothermal calorimetry experiments. S.Y., W.C., D.K., J.K., and S.B.P. cowrote the manuscript with input from all the other authors.

Notes

The authors declare no competing financial interest.

■ ACKNOWLEDGMENTS

This work was supported by a National Creative Research Initiative Grant (2014R1A3A2030423 to S.B.P.) and the Basic Science Research Program (RS-2023-00211336 and 2021R1A6A1A10044154 to J.K.) through the National Research Foundation of Korea (NRF) funded by the Korean Government (Ministry of Science; ICT), and the Basic Science Research Program through the National Research Foundation of Korea (NRF) funded by the Ministry of Education (RS-2023-00250268 to D.K.). S.Y. is grateful for NRF-Fostering Core Leaders of the Future Basic Science Program/Global Ph.D. Fellowship Program (2017H1A2A1045200). All the biological graphics were created with BioRender.com.

■ REFERENCES

(1) Herschel, J. F. W. On a case of superficial colour presented by a homogeneous liquid internally colourless. *Philos. Trans. R. Soc. London.* **1845**, *135*, 143−145.

(2) Stokes, G. G. On the change of refrangibility of light. *Philos. Trans. R. Soc. London.* **1852**, *142*, 463−562.

(3) Lee, Y.; Na, S.; Lee, S.; Jeon, N. L.; Park, S. B. Optimization of Seoul-Fluor-based lipid droplet bioprobes and their application in microalgae for bio-fuel study. *Mol. BioSyst.* **2013**, *9*, 952−956.

(4) Staderini, M.; Martin, M. A.; Bolognesi, M. L.; Menéndez, J. C. Imaging of β-amyloid plaques by near infrared fluorescent tracers: a new frontier for chemical neuroscience. *Chem. Soc. Rev.* **2015**, *44*, 1807−1819.

(5) Kim, J. H.; Gensch, T.; Zhao, D.; Stegemann, L.; Strassert, C. A.; Glorius, F. Rh^{III}-catalyzed C-H activation with pyridotriazole: direct access to fluorophores for metal-ion detection. *Angew. Chem., Int. Ed.* **2008**, *54*, 10975−10979.

(6) Sreejith, S.; Divya, K. P.; Ajayaghosh, A. A near-infrared squaraine dye as a latent ratiometric fluorophore for the detection of aminothiol content in blood plasma. *Angew. Chem., Int. Ed.* **2008**, *47*, 7883−7887.

(7) Jaska, C. A.; Piers, W. E.; McDonald, R.; Parvez, M. Synthesis, characterization, and fluorescence behavior of twisted and planar B_2N_2-quaterphenyl analogues. *J. Org. Chem.* **2007**, *72*, 5234−5243.

(8) Pohl, R.; Montes, V. A.; Shinar, J.; Anzenbacher, P. Red-green-blue emission from tris(5-aryl-8-quinolinolate)Al(III) complexes. *J. Org. Chem.* **2004**, *69*, 1723−1725.

(9) Kim, E.; Lee, S.; Park, S. B. A Seoul-Fluor-based bioprobe for lipid droplets and its application in image-based high throughput screening. *Chem. Commun.* **2012**, *48*, 2331−2333.

(10) Lee, H. Y.; Lee, J. J.; Park, J.; Park, S. B. Development of fluorescent glucose bioprobes and their application on real-time and quantitative monitoring of glucose uptake in living cells. *Chem._Eur. J.* **2011**, *17*, 143−150.

(11) Bosch, P.; García, V.; Bilen, B. S.; Sucunza, D.; Domingo, A.; Mendicuti, F.; Vaquero, J. J. Imidazopyridinium cations: A new family of azonia aromatic heterocycles with applications as DNA intercalators. *Dyes Pigm.* **2017**, *138*, 135−146.
(12) Yang, D.-T.; Radtke, J.; Mellerup, S. K.; Yuan, K.; Wang, X.; Wagner, M.; Wang, S. One-pot synthesis of brightly fluorescent Mes_2B-functionalized indolizine derivatives *via* cycloaddition reactions. *Org. Lett.* **2015**, *17*, 2486−2489.
(13) Saridakis, I.; Riomet, M.; Belleza, O. J. V.; Coussanes, G.; Singer, N. K.; Kastner, N.; Xiao, Y.; Smith, E.; Tona, V.; de la Torre, A.; et al. PyrAtes: Modular organic salts with large Stokes shifts for fluorescence microscopy. *Angew. Chem., Int. Ed.* **2024**, *63*, No. e202318127.
(14) Bakulina, O.; Merkt, F. K.; Knedel, T.-O.; Janiak, C.; Müller, T. J. J. Synthesis of water-soluble blue-emissive tricyclic 2-aminopyridinium salts by three-component coupling-(3 + 3)-anellation. *Angew. Chem., Int. Ed.* **2018**, *57*, 17240−17244.
(15) Chu, X.; Niu, Y.; Wang, X.; Lin, Y.; Li, F.; Ma, C. Regioselective oxidative cross-coupling reaction: Synthesis of imidazo[1,2-*a*]pyridine fluorophores. *Synthesis* **2021**, *53*, 1619−1628.
(16) Zhu, H.; Fan, J.; Du, J.; Peng, X. Fluorescent probes for sensing and imaging within specific cellular organelles. *Acc. Chem. Res.* **2016**, *49*, 2115−2126.
(17) Deng, H.; Lei, Q.; Wang, C.; Wang, Z.; Chen, H.; Wang, G.; Yang, N.; Huang, D.; Yu, Q.; Yao, M.; et al. A fluorogenic probe for predicting treatment response in non-small cell lung cancer with *EGFR*-activating mutations. *Nat. Commun.* **2022**, *13*, 6944.
(18) Loving, G.; Imperiali, B. A versatile amino acid analogue of the solvatochromic fluorophore 4-*N*,*N*-dimethylamino-1,8-naphthalimide: A powerful tool for the study of dynamic protein interactions. *J. Am. Chem. Soc.* **2008**, *130*, 13630−13638.
(19) Kim, H.; Jo, A.; Ha, J.; Lee, Y.; Hwang, Y. S.; Park, S. B. A pyrazolo[1,5-*b*]pyridine-fused pyrimidine based novel fluorophore and its bioapplication to probing lipid droplets. *Chem. Commun.* **2016**, *52*, 7822−7825.
(20) Yang, N. J.; Hinner, M. J. Gautier, A.; Hinner, M. J. *In Site-Specific Protein Labeling: methods and Protocols*; Springer: New York; 2015, pp. 2953.
(21) Metwally, S.; Stachewicz, U. Surface potential and charges impact on cell responses on biomaterials interfaces for medical applications. *Mater. Sci. Eng., C* **2019**, *104*, 109883.
(22) Benson, S.; Fernandez, A.; Barth, N. D.; de Moliner, F.; Horrocks, M. H.; Herrington, C. S.; Abad, J. L.; Delgado, A.; Kelly, L.; Chang, Z.; et al. SCOTfluors: Small, conjugatable, orthogonal, and tunable fluorophores for *in vivo* imaging of cell metabolism. *Angew. Chem., Int. Ed.* **2019**, *58*, 6911−6915.
(23) Toseland, C. P. Fluorescent labeling and modification of proteins. *J. Chem. Biol.* **2013**, *6*, 85−95.
(24) Jun, J. V.; Chenoweth, D. M.; Petersson, E. J. Rational design of small molecule fluorescent probse for biological applications. *Org. Biomol. Chem.* **2020**, *18*, 5747−5763.
(25) Kang, R.; Talamini, L.; D'Este, E.; Estevão, B. M.; De Cola, L.; Klopper, W.; Biedermann, F. Discovery of a size-record breaking green-emissive fluorophore: small, smaller, HINA. *Chem. Sci.* **2021**, *12*, 1392−1397.
(26) Sokolova, E. A.; Festa, A. A.; Golantsov, N. E.; Lukonina, N. S.; Ioffe, I. N.; Varlamov, A. V.; Voskressensky, L. G. Highly fluorescent pyrido[2,3-*b*]indolizine-10-carbonitriles through pseudo three-component reactions of *N*-(cyanomethyl)pyridinium salts. *Eur. J. Org. Chem.* **2019**, *2019*, 6770−6775.
(27) Martin, C.; Borreguero, C.; Kennes, K.; Van der Auweraer, M.; Hofkens, J.; de Miguel, G.; García-Frutos, E. M. Bipolar luminescent azaindole derivative exhibiting aggregation-induced emission for non-doped organic light-emitting diodes. *J. Mater. Chem. C* **2019**, *7*, 1222−1227.
(28) Merkel, L.; Hoesl, M. G.; Albrecht, M.; Schmidt, A.; Budisa, N. Blue fluorescent amino acids as *in vivo* building blocks for proteins. *ChemBiochem* **2010**, *11*, 305−314.
(29) Chen, Y.; Rich, R. L.; Gai, F.; Petrich, J. W. Fluorescent species of 7-azaindole and 7-azatryptophan in water. *J. Phys. Chem.* **1993**, *97*, 1770−1780.
(30) Zhao, S.-B.; Wang, S. Luminescence and reactivity of 7-azaindole derivatives and complexes. *Chem. Soc. Rev.* **2010**, *39*, 3142−3156.
(31) Negrerie, M.; Gai, F.; Bellefeuille, S.; Petrich, J. W. Photophysics of a novel optical probe: 7-azaindole. *J. Phys. Chem.* **1991**, *95*, 8663−8670.
(32) Kim, E.; Koh, M.; Lim, B. J.; Park, S. B. Emission wavelength prediction of a full-color-tunable fluorescent core skeleton, 9-aryl-1,2-dihydropyrrolo[3,4-*b*]indoliz-3-one. *J. Am. Chem. Soc.* **2011**, *133*, 6642−6649.
(33) Kim, E.; Koh, M.; Ryu, J.; Park, S. B. Combinatorial discovery of full-color-tunable emissive fluorescent probes using a single core skeleton, 1,2-dihydropyrrolo[3,4-*b*]indolizin-3-one. *J. Am. Chem. Soc.* **2008**, *130*, 12206−12207.
(34) Kim, E.; Lee, Y.; Lee, S.; Park, S. B. Discovery, understanding, and bioapplication of organic fluorophore: a case study with an indolizine-based novel fluorophore, Seoul-Fluor. *Acc. Chem. Res.* **2015**, *48*, 538−547.
(35) Lee, Y.; Jo, A.; Park, S. B. Rational improvement of molar absorptivity guided by oscillator strength: a case study with furoindolizine-based core skeleton. *Angew. Chem., Int. Ed.* **2015**, *54*, 15689−15693.
(36) Choi, E. J.; Kim, E.; Lee, Y.; Jo, A.; Park, S. B. Rational perturbation of the fluorescence quantum yield in emission-tunable and predictable fluorophores (Seoul-Fluors) by a facile synthetic method involving C-H activation. *Angew. Chem., Int. Ed.* **2014**, *53*, 1346−1350.
(37) Escudero, D. Revising intramolecular photoinduced electron transfer (PET) from first-principles. *Acc. Chem. Res.* **2016**, *49*, 1816−1824.
(38) Larsen, M. A. B.; Stephansen, A. B.; Alarousu, E.; Pittelkow, M.; Mohammded, O. F.; Sølling, T. I. Solvent-dependent dual fluorescence of the push-pull system 2-diethylamino-7-nitrofluorene. *Phys. Chem. Chem. Phys.* **2018**, *20*, 5942−5951.
(39) Lee, Y.; Cho, W.; Sung, J.; Kim, E.; Park, S. B. Monochromophoric design strategy for tetrazine-based colorful bioorthogonal probes with a single fluorescent core skeleton. *J. Am. Chem. Soc.* **2018**, *140*, 974−983.
(40) Chi, W.; Huang, L.; Wang, C.; Tan, D.; Xu, Z.; Liu, X. A unified fluorescence quenching mechanism of tetrazine-based luorogenic dyes: energy transfer to a dark state. *Mater. Chem. Front.* **2021**, *5*, 7012−7021.
(41) Wilfling, F.; Haas, J. T.; Walther, T. C.; Farese, R. V. J. Lipid droplet biogenesis. *Curr. Opin. Cell Biol.* **2014**, *29*, 39−45.
(42) Welte, M. A.; Gould, A. P. Lipid droplet functions beyond energy storage. *Biochim. Biophys. Acta* **2017**, *1862*, 1260−1272.
(43) Greenberg, A. S.; Coleman, R. A.; Kraemer, F. B.; McManaman, J. L.; Obin, M. S.; Puri, V.; Yan, Q.-W.; Miyoshi, H.; Mashek, D. G. The role of lipid droplets in metabolic disease in rodents and humans. *J. Clin. Invest.* **2011**, *121*, 2102−2110.
(44) Wang, H.; Lei, M.; Hsia, R. C.; Sztalryd, C. Analysis of lipid droplets in cardiac muscle. *Methods Cell Biol.* **2013**, *116*, 129−149.
(45) Farmer, B. C.; Walsh, A. E.; Kluemper, J. C.; Johnson, L. A. Lipid droplets in neurodegenerative disorders. *Front. Neurosci.* **2020**, *14*, 742.
(46) Lu, H.; Zhou, Q.; He, J.; Jiang, Z.; Peng, C.; Tong, R.; Shi, J. Recent advances in the development of protein-protein interactions modulators: mechanisms and clinical trials. *Signal Transduction Targeted Ther.* **2020**, *5*, 213.
(47) Shin, Y.-H.; Jeong, K.; Lee, J.; Lee, H. J.; Yim, J.; Kim, J.; Kim, S.; Park, S. B. Inhibition of ACE2-Spike interaction by an ACE2 binder suppresses SARS-CoV-2- Entry. *Angew. Chem., Int. Ed.* **2022**, *61*, No. e202115695.
(48) Lim, D.; Byun, W. G.; Koo, J. Y.; Park, S. B. Discovery of a small-molecule inhibitor of protein-microRNA interaction using

https://doi.org/10.1021/jacsau.4c00135
JACS Au 2024, 4, 2896−2906

binding assay with a site-specifically labeled Lin28. *J. Am. Chem. Soc.* **2016**, *138*, 13630−13638.
(49) Stormo, G. D.; Zhao, Y. Determining the specificity of protein-DNA interactions. *Nat. Rev. Genet.* **2010**, *11*, 751−760.
(50) Burslem, G. M.; Crews, C. M. Proteolysis-targeting chimeras as therapeutics and tools for biological discovery. *Cell* **2020**, *181*, 102−114.
(51) Gerry, C. J.; Schreiber, S. L. Unifying principles of bifunctional, proximity-inducing small molecules. *Nat. Chem. Biol.* **2020**, *16*, 369−378.
(52) Cho, W.; Won, S.; Choi, Y.; Yi, S.; Park, J. B.; Park, J.-G.; Kim, C. E.; Narayana, C.; Kim, J. H.; Yim, J.; et al. Targeted protein upregulation of STING for boosting the efficacy of immunotherapy. *Angew. Chem., Int. Ed.* **2023**, *62*, No. e202300978.
(53) Cheng, Z.; Kuru, E.; Sachdeva, A.; Vendrell, M. Fluorescent amino acids as versatile building blocks for chemical biology. *Nat. Rev. Chem.* **2020**, *4*, 275−290.
(54) Strizhak, A. V.; Postupalenko, V. Y.; Shvadchak, V. V.; Morellet, N.; Guittet, E.; Pivovarenko, V. G.; Klymchenko, A. S.; Mély, Y. Two-color fluorescent *L*-amino acid mimic of tryptophan for probing peptide-nucleic acid complexes. *Bioconjugate Chem.* **2012**, *23*, 2434−2443.
(55) Postupalenko, V. Y.; Zamotaiev, O. M.; Shvadchak, V. V.; Strizhak, A. V.; Pivovarenko, V. G.; Klymchenko, A. S.; Mély, Y. Dual-fluorescence *L*-amino acid reports insertion and orientation of melittin peptide in cell membranes. *Bioconjugate Chem.* **2013**, *24*, 1998−2007.
(56) Speight, L. C.; Muthusamy, A. K.; Goldberg, J. M.; Warner, J. B.; Wissner, R. F.; Willi, T. S.; Woodman, B. F.; Mehl, R. A.; Petersson, E. J. Efficient synthesis and *in vivo* incorporation of acridon-2-ylalanine, a fluorescent amino acid for lifetime and Forster resonance energy transfer/luminescence resonance energy transfer studies. *J. Am. Chem. Soc.* **2013**, *135*, 18806−18814.
(57) Wang, J.; Xie, J.; Schultz, P. G. A genetically encoded fluorescent amino acid. *J. Am. Chem. Soc.* **2006**, *128*, 8738−8739.
(58) Egan, A. J. F.; Cleverley, R. M.; Peters, K.; Lewis, R. J.; Vollmer, W. Regulation of bacterial cell wall growth. *Febs J.* **2017**, *284*, 851−867.
(59) Reese, A. E.; de Moliner, F.; Mendive-Tapia, L.; Benson, S.; Kuru, E.; Bridge, T.; Richards, J.; Rittichier, J.; Kitamura, T.; Sachdeva, A.; et al. Inserting "OFF-to-ON" BODIPY tags into cytokines: a fluorogenic interleukin IL-33 for real-time imaging of immune cells. *ACS Cent. Sci.* **2024**, *10*, 143−154.
(60) de Moliner, F.; Konienczna, Z.; Mendive-Tapia, L.; Saleeb, R. S.; Morris, K.; Gonzalez-Vera, J. A.; Kaizuka, T.; Grant, S. G. N.; Horrocks, M. H.; Vendrell, M. Small fluorogenic amino acids for peptide-guided background-free imaging. *Angew. Chem., Int. Ed.* **2023**, *62*, No. e202216231.
(61) Nimje, R. Y.; Vytla, D.; Kuppusamy, P.; Velayuthaperumal, R.; Jarugu, L. B.; Reddy, C. A.; Chikkananjaiah, N. K.; Rampulla, R. A.; Cavallaro, C. L.; Li, J.; et al. Synthesis of differentially protected azatryptophan analogs via $Pd_2(dba)_3$/XPhos catalyzed Negishi coupling of *N*-Ts azaindole halides with zinc derivative from Fmoc-protected *tert*-butyl (*R*)-2-amino-3-iodopropanoate. *J. Org. Chem.* **2020**, *85*, 11519−11530.
(62) Hilaire, M. R.; Ahmed, I. A.; Lin, C.-W.; Jo, H.; DeGrado, W. F.; Gai, F. Blue fluorescent amino acid for biological spectroscopy and microscopy. *Proc. Natl. Acad. Sci. U. S. A.* **2017**, *114*, 6005−6009.
(63) Talukder, P.; Chen, S.; Arce, P. M.; Hecht, S. M. Efficient asymmetric synthesis of tryptophan analogues having useful photophysical properties. *Org. Lett.* **2014**, *16*, 556−559.
(64) Williams, T. J.; Reay, A. J.; Whitwood, A. C.; Fairlamb, I. J. S. A mild and selective Pd-mediated methodology for the synthesis of highly fluorescent 2-arylated tryptophans and tryptophan-containing peptides: a catalytic role for Pd^0 nanoparticles? *Chem. Commun.* **2014**, *50*, 3052−3054.
(65) Pederson, S. W.; Albertsen, L.; Moran, G. E.; Levesque, B.; Pederson, S. B.; Bartels, L.; Wapenaar, H.; Ye, F.; Zhang, M.; Bowen, M. E.; et al. Site-specific phosphorylation of PSD-95 PDZ domains reveals fine-tuned regulation of protein-protein interactions. *ACS Chem. Biol.* **2017**, *12*, 2313−2323.
(66) Sainlos, M.; Iskenderian, W. S.; Imperiali, B. A general screening strategy for peptide-based fluorogenic ligands: probes for dynamic studies of PDZ domain-mediated interactions. *J. Am. Chem. Soc.* **2009**, *131*, 6680−6682.
(67) Deng, F.; Price, M. G.; Davis, C. F.; Mori, M.; Burgess, D. L. Stargazin and other transmembrane AMPA receptor regulating proteins interact with synaptic scaffolding protein MAGI-2 in brain. *J. Neurosci.* **2006**, *26*, 7875−7884.
(68) Dakoji, S.; Tomita, S.; Karimzadegan, S.; Nicoli, R. A.; Bredt, D. S. Interaction of transmembrane AMPA receptor regulatory proteins with multiple membrane associated guanylate kinases. *Neuropharmacology* **2003**, *45*, 849−856.
(69) Coley, A. A.; Gao, W.-J. PSD95: A synaptic protein implicated in schizophrenia or autism? *Prog. Neuro-Psychopharmacol. Biol. Psychiatry* **2018**, *82*, 187−194.

https://doi.org/10.1021/jacsau.4c00135
JACS Au 2024, 4, 2896−2906